# Source model of the 16 September 2015 Illapel, Chile, $M_w$ 8.4 earthquake based on teleseismic and tsunami data

**Mohammad Heidarzadeh[1], Satoko Murotani[2], Kenji Satake[1], Takeo Ishibe[1], and Aditya Riadi Gusman[1]**

[1]Earthquake Research Institute, University of Tokyo, Tokyo, Japan, [2]National Museum of Nature and Science, Tsukuba, Japan

**Abstract** We proposed a source model for the 16 September 2015 Illapel (Chile) tsunamigenic earthquake using teleseismic and tsunami data. The 2015 epicenter was at the northernmost of the aftershocks zone of the 2010 $M_w$ 8.8 Maule earthquake. Teleseismic body wave inversions and tsunami simulations showed optimum rupture velocities of 1.5–2.0 km/s. The agreement between observed and synthetic waveforms was quantified using normalized root-mean-square (NRMS) misfit. The variations of NRMS misfits were larger for tsunami data compared to the teleseismic data, because tsunami waveforms are more sensitive to the spatial distribution of slip. The large-slip area was 80 km (along strike) × 100 km (along dip) with an average slip of 5.0 m and depth of 12–33 km, located ~70 km to the northwest of the epicenter. We obtained a seismic moment of $4.42 \times 10^{21}$ Nm equivalent to $M_w$ 8.4. Results may indicate a northward stress transfer from the 2010 Maule earthquake.

## 1. Introduction

A transoceanic tsunami was generated in the Pacific Ocean on 16 September 2015 following a large $M_w$ 8.4 earthquake offshore Illapel, Chile. The earthquake was located at 71.654°W and 31.570°S offshore the city of Illapel (Chile) at the depth of 25.0 km with the origin time of 22:54:33 UT by the United States Geological Survey (USGS). A moment magnitude ($M_w$) of 8.3 was assigned by USGS, but the teleseismic analyses (discussed later) resulted in an $M_w$ 8.4; hence, we use $M_w$ 8.4 hereafter. According to the Pacific Tsunami Warning Center and the Japan Meteorological Agency, the tsunami reached the farthest coastlines within the Pacific basin with zero-to-crest tide gauge amplitudes of up to 78 cm along Japan, ~90 cm in Hilo (Hawaii), 43.5 cm in Chatham (New Zealand), ~20 cm in Vanuatu, and ~10 cm in Port Kembla (Australia). In the near field, the tsunami amplitudes on tide gauges were ~2 m with a maximum value of 4.7 m registered in Coquimbo (Figure 1a). The distribution of large (>1 m) coastal wave amplitudes along ~1000 km segment of the Chilean coast is a characteristic of tectonic tsunamis [*Okal and Synolakis*, 2004]. According to news reports, extensive inundation and damage were reported in coastal cities including Coquimbo located ~100 km to the north of the epicenter. A massive and timely evacuation was conducted in the coastal areas engaging around one million coastal residents. The earthquake left at least 13 people dead. No deaths were reported due to the tsunami, possibly because of the timely tsunami warnings and evacuations.

Offshore Chile lies one of the world's most seismically active areas accommodating the Chilean subduction zone which is the result of subduction of the Nazca Plate beneath the South American Plate at a rate of 6.6 cm/yr [*Moreno et al.*, 2010] (Figures 1 and S1 in the supporting information). The region is frequently struck by large earthquakes including 13 $M > 8$ events since 1900 A.D. and consequent tsunamis (Figure S1). The Chilean subduction zone is a major source for transoceanic tsunamis within the Pacific Basin. The largest ever recorded earthquake ($M_w$ 9.5) occurred in this subduction zone in 1960 [*Kanamori*, 1977] which was followed by a destructive trans-Pacific tsunami [*Plafker and Savage*, 1970; *Fujii and Satake*, 2013]. The most recent deadly tsunami offshore Chile occurred on 27 February 2010 following the $M_w$ 8.8 Maule earthquake leaving a death toll of more than 500 as a result of both earthquake and tsunami [*Lorito et al.*, 2011; *Fritz et al.*, 2011; *Rabinovich et al.*, 2013; *Yamazaki and Cheung*, 2011; *Fujii and Satake*, 2013]. The distribution of aftershocks suggests that the rupture of the recent 16 September 2015 Illapel earthquake started from the northernmost limit of that from the 2010 Maule earthquake and propagated northward (Figure 1d). On 1 April 2014, another trans-Pacific tsunami was generated due to the $M_w$ 8.2 Iquique earthquake located ~1000 km to the north of the recent earthquake (Figure 1) [*Lay et al.*, 2014; *Gusman et al.*, 2015; *Yagi et al.*, 2014; *An et al.*, 2014; *Heidarzadeh et al.*, 2015a].
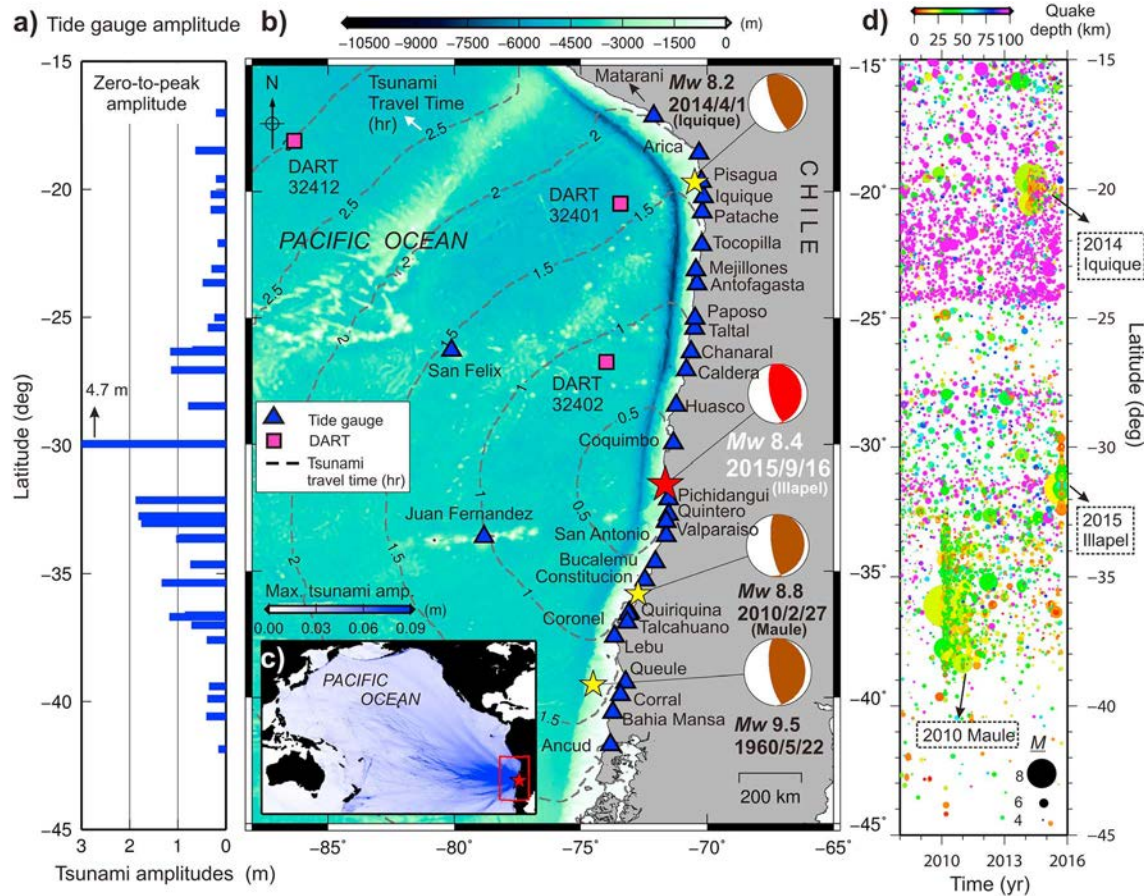
**Figure 1.** (a) Zero-to-crest tsunami amplitudes recorded on tide gauge stations due to the 2015 Illapel tsunami. (b) Epicenters of major tsunamigenic earthquakes and locations of DART and tide gauge stations used in this study. Focal mechanism of the 1960 $M_w$ 9.5 earthquake is from *Fujii and Satake* [2013], whereas other focal mechanisms are from the Global centroid moment tensor (CMT) catalog. Tsunami travel times (in hours) are shown by dashed lines for the 2015 Illapel tsunami. (c) Maximum tsunami amplitudes from our basin-wide tsunami simulations due to the 16 September Illapel earthquake. (d) Space (latitude)-time plot of earthquakes along the Chilean subduction zone since 2008. A logarithmic scale is used for earthquake magnitude. The hypocenters are from the USGS National Earthquake Information Center (NEIC) catalog.

Here we used both teleseismic and tsunami data and applied teleseismic body wave inversions, seismicity analysis, and tsunami simulations to study the 2015 $M_w$ 8.4 Illapel earthquake and consequent tsunami. Our objectives were the following: (1) to propose a source model which is consistent with both seismic and tsunami data and (2) to examine possible relationship between the 2015 Illapel and 2010 Maule earthquakes.

## 2. Methodology and Data

Our method was a combination of teleseismic inversions and forward tsunami simulations. For studying source models of tsunamigenic earthquakes, seismic data provide stable results in time domain, whereas tsunami data deliver spatially stable results, because seismic waves travel much faster than tsunami waves [*Satake*, 1987]. Hence, a combination of teleseismic and tsunami records is suitable to achieve source models that are stable both temporally and spatially. This methodology has been recently applied to some tsunamigenic earthquakes [e.g., *Lay et al.*, 2014; *Gusman et al.*, 2015; and *Heidarzadeh et al.*, 2015b].

The data consisted of 62 teleseismic and 33 tsunami records. The teleseismic $P$ wave vertical components recorded at distances between 30° and 100° from the epicenter (Figure S2) were provided by the Incorporated Research Institutions for Seismology. Band-pass filters with a frequency band between 0.003 and 1.0 Hz were applied to the teleseismic waveforms. For tsunami records, 3 were recorded by Deep-ocean Assessment and Reporting of Tsunamis (DART) [*Kanoglu et al.*, 2015; *Synolakis and Bernard*, 2006] and 30 were recorded at coastal tide gauges. All tsunami records had a sampling interval of 1 min. To detide the tsunami records, we estimated the tides by polynomial fitting; then the estimated tides were eliminated from the records.
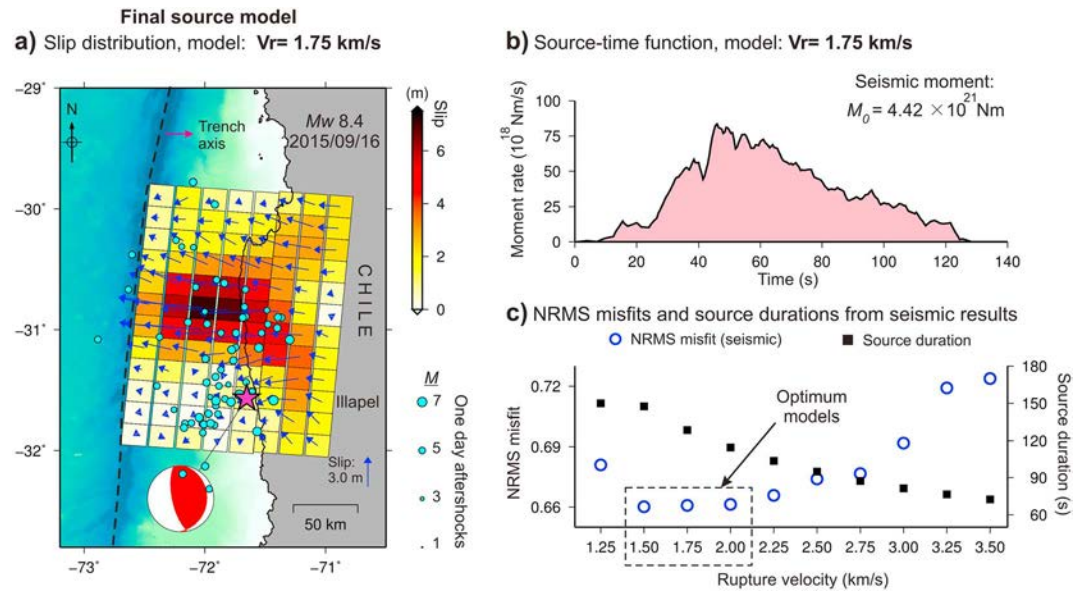
**Figure 2.** Final source model for the Illapel earthquake. (a) Slip distributions for the final source model (i.e., model $V_r$ = 1.75 km/s). Dimensions of each subfault are 20 km × 20 km. Cyan circles are 1 day aftershocks. Blue arrows show the amount and direction of slip on each subfault. Focal mechanism is from Global CMT catalog. (b) Source time function (moment rate function) for the final source model. (c) Comparison of NRMS misfit (left scale) and total source duration (right scale) for different rupture velocities.

Teleseismic body wave inversions were performed by applying a multi–time window inversion method based on *Kikuchi and Kanamori* [1991] to obtain source time (moment rate) function and slip distribution. Synthetic seismograms at far-field stations were computed using the method by *Kikuchi and Kanamori* [1982] and were used as Green's functions. The velocity structure based on ak135 and CRUST 2.0 [*Kennett et al.*, 1995; *Bassin et al.*, 2000] was adopted to compute teleseismic Green's functions. We used a total number of 96 subfaults in a 12 (along strike) × 8 (along dip) grid for teleseismic inversions (Figure 2a). The dimensions of each subfault were 20 km × 20 km. The top depths and dip angles of subfaults were in the ranges of 9.5–48.2 km and 7.0–23.1°, respectively, according to the SLAB1.0 subduction zone model [*Hayes et al.*, 2012]. The strike angle was 5° for all subfaults. For teleseismic inversions, the maximum rupture duration was 15.0 s for each subfault which was a combination of four overlapping triangles having 6.0 s of duration and 3.0 s of overlaps. We varied the rupture velocity ($V_r$) from 1.25 to 3.5 km/s using 0.25 km/s steps which resulted in 10 solutions. Our method for teleseismic body wave inversion was different from the typical one assuming a single maximum rupture front velocity. We varied rupture front velocity in the range of 1.25–3.5 km/s and estimated slip distribution for each model to examine how well they agree with tsunami data [*Gusman et al.*, 2015; *Heidarzadeh et al.*, 2015b].

Numerical simulations of tsunami propagation were conducted applying the model by *Satake* [1995] which is based on the linear shallow-water equations. To examine possible nonlinear effects on the tsunami waves recorded at the tide gauge stations, we performed nonlinear tsunami simulations for the final source model (results in next section). We used the 30 arc sec General Bathymetric Chart of the Oceans (GEBCO)-2014 bathymetric data in this study [*Intergovernmental Oceanographic Commission et al.*, 2014]. A single uniform grid was employed for simulations. The time step was 1.0 s to satisfy the stability condition of the finite difference method. The dislocation formulas by *Okada* [1985] were used to calculate initial seafloor deformation. We used the tsunami travel time program by *Geoware* [2011].

To compare the synthetic and observed waveforms, we used the normalized root-mean-square (NRMS) misfit defined as below:

$$NRMS_k = \frac{\sqrt{\sum_{i=1}^{N}(obs_i - sim_i)^2}}{\sqrt{\sum_{i=1}^{N}(obs_i - \overline{obs})^2}} \qquad (1)$$

$$NRMS\ misfit = \frac{\sum_{k=1}^{M} NRMS_k}{M} \qquad (2)$$

where $NRMS_k$ is the normalized root-mean-square misfit for the $k$th station, $i = 1, 2, \ldots, N$ refers to the sampled waveform, and $N$ is the number of sampling records at each station; $obs_i$ and $sim_i$ are observed and synthetic waveforms, respectively; $\overline{obs}$ is the average of the observed waveforms at each station, $k = 1, 2, \ldots, M$ refers to the stations, and $M$ is the number of stations. In other words, the final NRMS misfit value (i.e., "NRMS misfit" in equation (2)) is the average value of misfits from all stations for teleseismic or tsunami waveforms. Equation (1) is inspired by the NRMS error of *Mathworks* [2015]. According to equation (1), if the agreement between observations and simulations is perfect, the NRMS misfit is 0, and for the worst case, it is $+\infty$. Since the NRMS misfit is a normalized criterion, the NRMS misfit values from teleseismic and tsunami waveforms are directly comparable. For tsunami waveforms, we used only the first wave cycle at each station, whereas the full record was used for teleseismic waveforms for NRMS misfit calculations. To calculate NRMS misfit for tsunami, we selected stations where arrival time differences between simulations and observations were small (3 min or less), because large arrival time differences introduce large errors in NRMS misfit calculations. A tsunami travel time difference of up to 5 min have been reported for coastal tide gauges between simulations using coarse bathymetry (GEBCO 30 arc sec bathymetry) and using high-resolution bathymetry (1 arc sec bathymetry) [*Heidarzadeh and Satake*, 2014]. As the 30 arc sec bathymetry data were used here for tsunami simulations, arrival time differences between simulations and observations were expected at some stations and such stations were excluded from NRMS misfit calculations.

## 3. Source Model

Teleseismic inversion considering different rupture velocities resulted in 10 slip distributions (see Figure S3 for all 10 slip distributions and Figure S4 for snapshots). Results showed that the synthetic teleseismic waveforms from different slip models were very similar. Examples of synthetic waveforms from teleseismic inversions using two rupture velocities of 1.75 and 3.0 km/s are shown in Figures S5 and S6. The estimated source time functions for different $V_r$ had common peaks at ~50 s with maximum values of about 65 to $85 \times 10^{18}$ Nm/s, while the total source duration became longer for smaller $V_r$ (Figure 2c). By increasing rupture velocity from 1.50 to 3.5 km/s, the total source time duration decreased from ~150 to ~70 s (Figure S7). The slip distributions changed for various models. By increasing $V_r$, the rupture areas moved out of the epicenter, while the maximum slip values decreased by a factor of up to 2 (Figure S3). A trade-off was seen between NRMS misfit and source duration (Figure 2c). Three models of $V_r = 1.5$, 1.75, and 2.0 km/s showed similar NRMS misfits of 0.6602, 0.6608, and 0.6613, respectively, which were the optimum models from the teleseismic inversions (Figure 2c). To compare our results with those of the typical teleseismic inversion, we performed inversion using $V_r = 3.5$ km/s and by considering a rupture duration of 45 s (Figure S8). Results showed that slip distribution is similar to our models with $V_r = 1.75$–2.25 km/s, but the maximum slip is smaller than those of our models.

We performed tsunami simulations for all slip models (see Figures S10–S19 for tsunami simulations for all 10 models). Results showed that unlike teleseismic results, the synthetic tsunami waveforms clearly changed for various models. According to Figures S11, S17, and S19, the simulated tsunami waveforms at some stations from model $V_r = 1.5$ km/s were twice larger than those from model $V_r = 3.0$ km/s and were around 3 times larger than those from the model $V_r = 3.5$ km/s. This is because tsunami waveforms and amplitudes are dictated by the shape and amounts of seafloor deformation which were strongly varying in this study for different $V_r$ (see Figure S9 for seafloor deformations for all 10 slip models). We calculated NRMS misfit between observed and synthetic tsunami waveforms which gave the minimum value for model with $V_r = 1.75$ km/s (Figure 3b). Sixteen stations (Figure 3c), which had negligible travel time differences between simulations and observation, were used for NRMS misfit calculations. The NRMS values for each station (equation (1)) and for all slip models are shown in Figures S10–S19. For example, at Huasco, the simulated waveform from model $V_r = 1.75$ km/s is very similar to the observation in terms of amplitude and period; but it gives a large NRMS value of 1.67 because of the arrival time difference (Figure S12). The simulated waveform from model $V_r = 3.50$ km/s gives smaller NRMS value of 1.34 at this station although the amplitude of simulated waveform is smaller than both the 1.75 km/s model and the observation (Figure S19). NRMS misfit values from teleseismic waves were less variable than those for tsunami results (Figure 3b). According to Figure 3b, three models of $V_r = 1.5$, 1.75, and 2.0 km/s gave optimum NRMS misfits for both teleseismic and tsunami simulations. Among these three models, the best one was $V_r = 1.75$ km/s as it gave the minimum NRMS
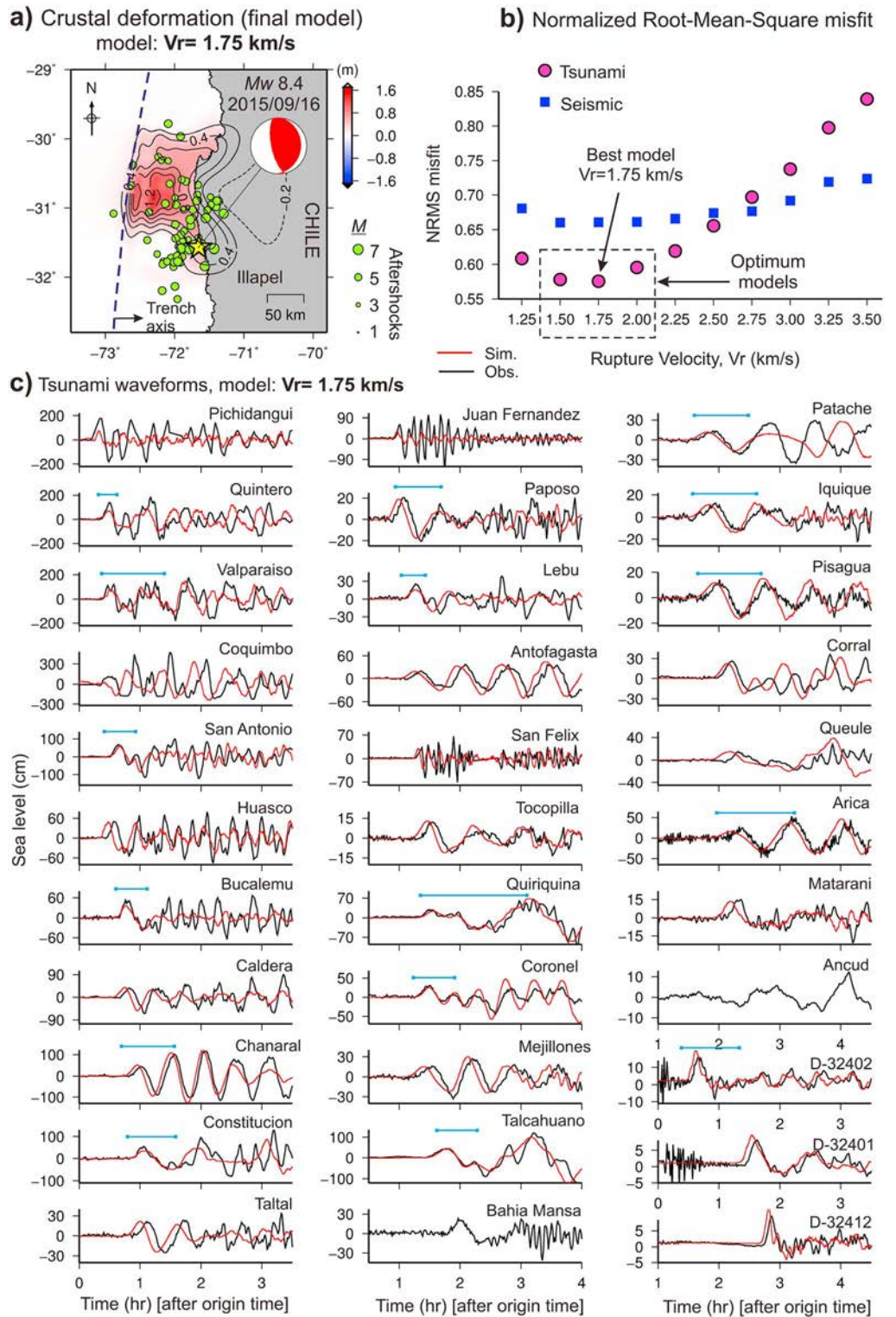
**Figure 3.** (a) Crustal deformation from the final model ($V_r$ = 1.75 km/s). The contours start with 0.2 m having 0.2 m intervals. Solid and dashed contours represent uplift and subsidence, respectively. Aftershocks within 1 day from the origin time are shown by green circles. (b) Normalized root-mean-square (NRMS) misfits calculated for the synthetic and observed teleseismic and tsunami waveforms. Sixteen stations were used for NRMS misfit calculations for tsunami which are marked by cyan horizontal lines on top of them. (c) The synthetic (red) and observed (black) tsunami waveforms for final slip model ($V_r$ = 1.75 km/s). Two stations, i.e., Bahia-Mansa and Ancud, were located out of our computational domain; hence, simulated waveforms are not available for them.

misfit for tsunami simulations. Figure 2a shows the slip distribution of this final model and Figure 3c presents the synthetic tsunami waveforms from this final model (i.e., $V_r = 1.75$ km/s). Tsunami simulations using nonlinear equations showed that the synthetic waveforms were very similar to those obtained from linear simulations (Figure S20).

In summary, the final source model had a $V_r$ of 1.75 km/s (Figures 2a, 2b, and 3a). This model had a rupture duration of ~125 s. The peak of the source time function occurred at ~50 s (Figure 2b). The rake angle distribution showed that the slip on most subfaults indicated pure reverse (thrust) fault motion (Figure 2a). By defining the large-slip region as those subfaults with slip of >3.35 m (1.5 times the average slip of all subfaults) [*Murotani et al.*, 2013], the large-slip area was about 80 km (along strike) × 100 km (along dip) with an average slip of 5.0 m. The center of large-slip area was located ~70 km to the northwest of the epicenter. This confirms that the rupture propagated from the epicenter to the northwest direction. This source model had a seismic moment of $4.42 \times 10^{21}$ N m ($M_w$ 8.4). The maximum crustal uplift and subsidence were ~1.4 and ~0.4 m, respectively (Figure 3a). Because the coseismically subsided area was limited inland (Figure 3a), all tsunami waveforms showed initial elevation waves.

## 4. Discussion

The final slip model inferred from teleseismic body waves and tsunami waveforms showed that almost all of the slip during the 2015 Illapel earthquake occurred toward the north of the epicenter (Figures 2a and S3). The final source model indicates that the large-slip area of 80 km (along strike) × 100 km (along dip) was located ~70 km to the northwest of the epicenter. The large-slip area was ~20% of the total rupture area (i.e., the area of all subfaults with nonzero slip) and its average slip (5.0 m) was about twice of the average slip of the entire fault (2.23 m); similar to other subduction zone earthquakes [*Murotani et al.*, 2013]. The depth of the large-slip area was in the range of 12–33 km. The aftershock distribution, both within 1 day (Figure 2) and 14 days (Figure 4a) of the main shock, revealed that most of them were located near the epicenter within a distance of ~50 km. Relatively smaller number of aftershocks occurred in the large-slip area (Figure 4a). Near the epicenter of the 2015 Illapel earthquake, a great earthquake with $M_w$ 8.1 occurred in 1943 (Figure 4). The time interval since this event is 72 years, during which period the total slip deficit would be ~5 m considering the plate convergence rate of 6.6 cm/yr [*Moreno et al.*, 2010]. The average slip of 5.0 m in the large-slip area indicates that the 2015 Illapel earthquake fully released the strain accumulated during the interseismic period.

Figure 4a shows the slip distribution of the recent 2015 Illapel earthquake together with that of 2010 Maule earthquake from *Fujii and Satake* [2013] with respective seismicity. It can be seen that the two rupture areas are clearly divided at the latitude of ~32.5°S. This boundary region experienced 18 earthquakes with $M > 5$ since 2010 Maule earthquake (Figure 4b). This is possibly due to the coseismically transferred stress from the Maule earthquake to the north. In general, Figure 4 indicates a northward stress transfer from the Maule earthquake which induced active seismicity at the boundary area (around latitude 32.5°S) leading to the 2015 Illapel earthquake. While the epicentral area of the 2015 Illapel earthquake ruptured after 72 years (i.e., since the 1943 event), the boundary area to the south of the Ilapel event did not experience any large earthquake since the 1906 event (i.e., after 109 years) (Figure 4a). The reason why northward stress transfer from the 2010 Maule earthquake resulted in a large earthquake in the area of the 1943 earthquake and not in the area of the 1906 event could be due to heterogeneity in frictional strength along the plate boundary (Y. Tanioka, written communication, 2015).

To further confirm the existence of the boundary region, i.e., the gap between the source regions of the 2015 Illapel and the 2010 Maule earthquakes, we performed teleseismic body wave inversions and tsunami simulations for an extended fault which covers the areas to the south of the epicenter (Figure S21). By extending the fault area to the south, a new patch of slip was revealed through teleseismic inversions (Figure S21b) which did not exist in our final model (Figure 2a). However, tsunami simulations showed that the slip distribution from the extended fault is not consistent with the tsunami observations. Due to this new slip in the south of the epicenter, a small elevation wave appeared in the synthetic tsunami waveforms which arrives earlier than the actual tsunami arrival times (blue arrows in Figure S21c). Tsunami backward ray tracing also confirmed that the earthquake source area was limited to the north of the epicenter (Figure S22).
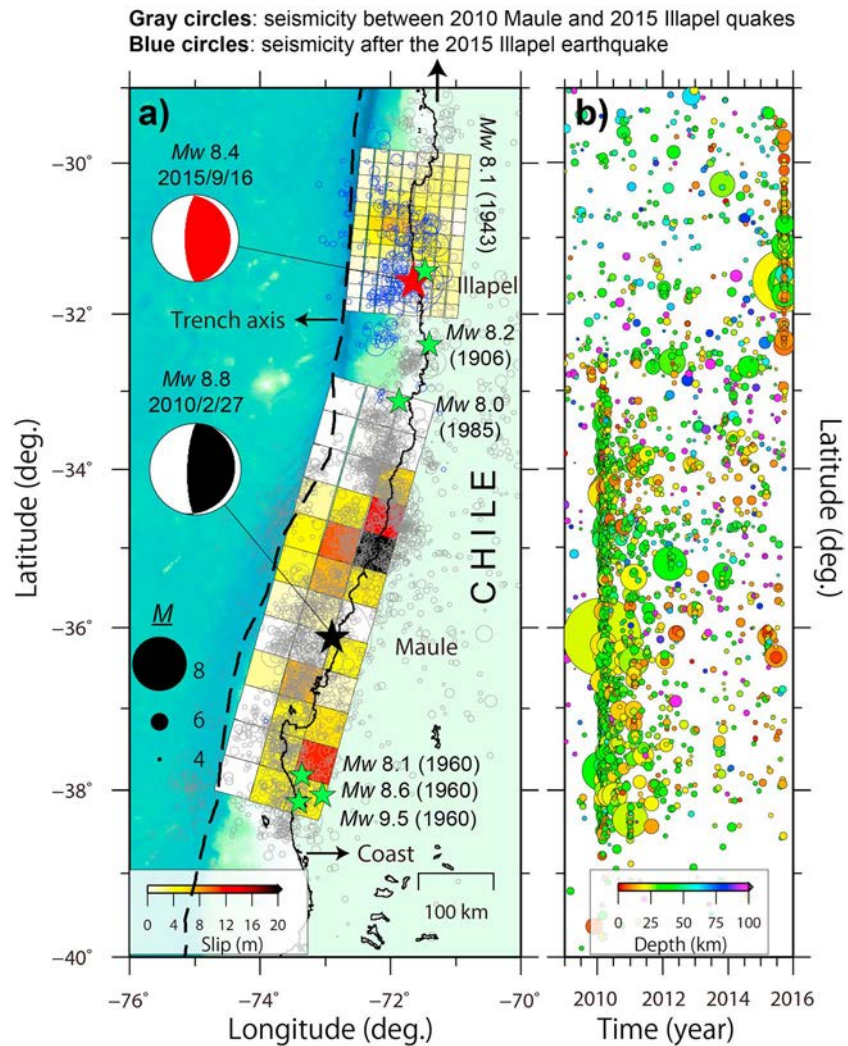
**Figure 4.** (a) Slip distributions of the recent 2015 Illapel and 2010 Maule earthquakes along with the seismicity of the region since 2010 Maule earthquake. The slip distribution of the Maule earthquake is from *Fujii and Satake* [2013]. The gray open circles are seismicity between Maule and Illapel earthquakes. The blue open circles represent seismicity after the Illapel earthquake. (b) Space (latitude)-time plot of earthquakes in the region since 2009. A logarithmic scale is used for earthquake magnitude. The hypocenters are from the USGS National Earthquake Information Center (NEIC) catalog.

## 5. Conclusions

The 16 September 2015 $M_w$ 8.4 Illapel tsunamigenic thrust earthquake was studied using teleseismic and tsunami data. Main findings are as follows:

1. The tsunami registered zero-to-crest amplitudes of ~2 m on the near-field tide gauges with a maximum amplitude of 4.7 m on the Coquimbo tide gauge located ~100 km to the north of the epicenter. The tsunami amplitude was 10.9 cm on the nearest DART station (DART 32402), located ~450 km to the northwest of the epicenter.

2. Ten slip models from teleseismic inversions with rupture velocities ($V_r$) from 1.25 to 3.5 km/s yielded similar synthetic waveforms. Normalized root-mean-square (NRMS) misfits between synthetic and observed waveforms were in a small range of 0.6602–0.6613 for three models of $V_r = 1.5$, 1.75, and 2.0 km/s, which were the optimum models from teleseismic results.

3. Simulated tsunami waveforms clearly changed for various models giving larger NRMS misfit variations compared to those from teleseismic waveforms. NRMS misfits from tsunami simulation also preferred

slow rupture velocities in the range 1.5–2.0 km/s as the optimum models. Among these three models, the best one was $V_r = 1.75$ km/s, as it gave the minimum NRMS misfit for tsunami waveforms.

4. For our final model ($V_r = 1.75$ km/s), the rupture duration was ~125 s and the peak of the source time function occurred at ~50 s. The large-slip area was 80 km (along strike) × 100 km (along dip), with an average slip of ~5.0 m, whose center was located ~70 km from the trench axis and ~70 km to the northwest of the epicenter. The depth of the large-slip area was in the range 12–33 km. The final source model had a seismic moment of $4.42 \times 10^{21}$ N m ($M_w$ 8.4).

5. The rupture areas of the 2010 Maule and 2015 Illapel earthquakes were clearly divided at the latitude of ~32.5°S. This boundary region experienced 18 earthquakes with $M > 5$ since the 2010 event. This may indicate a northward stress transfer from 2010 which induced active seismicity at the boundary area leading to the 2015 $M_w$ 8.4 Illapel earthquake.

## References

An, C., I. Sepúlveda, and P. L.-F. Liu (2014), Tsunami source and its validation of the 2014 Iquique, Chile earthquake, *Geophys. Res. Lett.*, *41*, 3988–3994, doi:10.1002/2014GL060567.

Bassin, C., G. Laske, and G. Masters (2000), The current limits of resolution for surface wave tomography in North America, *Eos Trans. AGU*, *81*, F897.

Fritz, H. M., et al. (2011), Field survey of the 27 February 2010 Chile tsunami, *Pure Appl. Geophys.*, *168*(11), 1989–2010.

Fujii, Y., and K. Satake (2013), Slip distribution and seismic moment of the 2010 and 1960 Chilean earthquakes inferred from tsunami waveforms and coastal geodetic data, *Pure Appl. Geophys.*, *170*(9–10), 1493–1509.

Geoware (2011), The tsunami travel times (TTT). [Available at http://www.geoware-online.com/tsunami.html.]

Gusman, A. R., S. Murotani, K. Satake, M. Heidarzadeh, E. Gunawan, S. Watada, and B. Schurr (2015), Fault slip distribution of the 2014 Iquique, Chile, earthquake estimated from ocean-wide tsunami waveforms and GPS data, *Geophys. Res. Lett.*, *42*, 1053–1060, doi:10.1002/2014GL062604.

Hayes, G. P., D. J. Wald, and R. L. Johnson (2012), Slab1.0: A three-dimensional model of global subduction zone geometries, *J. Geophys. Res.*, *117*, B01302, doi:10.1029/2011JB008524.

Heidarzadeh, M., and K. Satake (2014), Possible sources of the tsunami observed in the northwestern Indian Ocean following the 2013 September 24 $M_w$ 7.7 Pakistan inland earthquake, *Geophys. J. Int.*, *199*(2), 752–766.

Heidarzadeh, M., K. Satake, S. Murotani, A. R. Gusman, and S. Watada (2015a), Deep-water characteristics of the trans-Pacific tsunami from the 1 April 2014 $M_w$ 8.2 Iquique, Chile earthquake, *Pure Appl. Geophys.*, *172*(3–4), 719–730.

Heidarzadeh, M., A. R. Gusman, T. Harada, and K. Satake (2015b), Tsunamis from the 29 March and 5 May 2015 Papua New Guinea earthquake doublet ($M_w$ 7.5) and tsunamigenic potential of the New Britain trench, *Geophys. Res. Lett.*, *42*, 5958–5965, doi:10.1002/2015GL064770.

Intergovernmental Oceanographic Commission, IHO, and BODC (2014), Centenary edition of the GEBCO digital Atlas, published on CD-ROM on behalf of the Intergovernmental Oceanographic Commission and the International Hydrographic Organization as part of the General Bathymetric Chart of the Oceans, British Oceanographic Data Centre, Liverpool, U. K.

Kanamori, H. (1977), The energy release in great earthquakes, *J. Geophys. Res.*, *82*(20), 2981–2987, doi:10.1029/JB082i020p02981.

Kanoglu, U., V. Titov, E. Bernard, and C. Synolakis (2015), Tsunamis: Bridging science, engineering and society, *Philos. Trans. R. Soc. A*, *373*(2053), doi:10.1098/rsta.2014.0369.

Kennett, B. L. N., E. R. Engdahl, and R. Buland (1995), Constraints on seismic velocities in the Earth from travel times, *Geophys. J. Int.*, *122*, 108–124.

Kikuchi, M., and H. Kanamori (1982), Inversion of complex body waves, *Bull. Seismol. Soc. Am.*, *72*, 491–506.

Kikuchi, M., and H. Kanamori (1991), Inversion of complex body waves—III, *Bull. Seismol. Soc. Am.*, *81*(6), 2335–2350.

Lay, T., H. Yue, E. E. Brodsky, and C. An (2014), The 1 April 2014 Iquique, Chile, $M_w$ 8.1 earthquake rupture sequence, *Geophys. Res. Lett.*, *41*, 3818–3825, doi:10.1002/2014GL060238.

Lorito, S., F. Romano, S. Atzori, X. Tong, A. Avallone, J. McCloskey, M. Cocco, E. Boschi, and A. Piatanesi (2011), Limited overlap between the seismic gap and coseismic slip of the great 2010 Chile earthquake, *Nat. Geosci.*, *4*(3), 173–177.

Mathworks (2015), *MATLAB and Statistics Toolbox Release 2012b*, The MathWorks, Inc, Natick, Mass.

Moreno, M., M. Rosenau, and O. Oncken (2010), 2010 Maule earthquake slip correlates with pre-seismic locking of Andean subduction zone, *Nature*, *467*(7312), 198–202.

Murotani, S., K. Satake, and Y. Fujii (2013), Scaling relations of seismic moment, rupture area, average slip, and asperity size for $M \sim 9$ subduction-zone earthquakes, *Geophys. Res. Lett.*, *40*, 5070–5074, doi:10.1002/grl.50976.

Okada, Y. (1985), Surface deformation due to shear and tensile faults in a half-space, *Bull. Seismol. Soc. Am.*, *75*, 1135–1154.

Okal, E. A., and C. E. Synolakis (2004), Source discriminants for near-field tsunamis, *Geophys. J. Int.*, *158*(3), 899–912.

Plafker, G., and J. C. Savage (1970), Mechanism of the Chilean earthquakes of May 21 and 22, 1960, *Geol. Soc. Am. Bull.*, *81*(4), 1001–1030.

Rabinovich, A. B., R. E. Thomson, and I. V. Fine (2013), The 2010 Chilean tsunami off the west coast of Canada and the northwest coast of the United States, *Pure Appl. Geophys.*, *170*(9–10), 1529–1565.

Satake, K. (1987), Inversion of tsunami waveforms for the estimation of a fault heterogeneity: Method and numerical experiments, *J. Phys. Earth*, *35*(3), 241–254.

Satake, K. (1995), Linear and nonlinear computations of the 1992 Nicaragua earthquake tsunami, *Pure Appl. Geophys.*, *144*, 455–470.

Synolakis, C. E., and E. N. Bernard (2006), Tsunami science before and beyond Boxing Day 2004, *Philos. Trans. R. Soc. London A*, *364*(1845), 2231–2265.

Wessel, P., and W. H. F. Smith (1998), New, improved version of Generic Mapping Tools released, *Eos Trans. AGU*, *79*(47), 579.

Yagi, Y., R. Okuwaki, B. Enescu, S. Hirano, Y. Yamagami, S. Endo, and T. Komoro (2014), Rupture process of the 2014 Iquique Chile earthquake in relation with the foreshock activity, *Geophys. Res. Lett.*, *41*, 4201–4206, doi:10.1002/2014GL060274.

Yamazaki, Y., and K. F. Cheung (2011), Shelf resonance and impact of near-field tsunami generated by the 2010 Chile earthquake, *Geophys. Res. Lett.*, *38*, L12605, doi:10.1029/2011GL047508.